The local far-infrared galaxy colour–luminosity distribution: a reference for BLAST and *Herschel*/SPIRE submillimetre surveys

E. L. Chapin,[1]★ D. H. Hughes[2] and I. Aretxaga[2]

[1]*Department of Physics and Astronomy, University of British Columbia, 6224 Agricultural Road, Vancouver, B.C. V6T 1Z1, Canada*
[2]*Instituto Nacional de Astrofísica, Óptica y Electrónica (INAOE), Aptdo. Postal 51 y 216, Puebla, Mexico*

ABSTRACT

We measure the local galaxy far-infrared (FIR) 60 to 100 μm colour–luminosity distribution using an all-sky *IRAS* survey. This distribution is an important reference for the next generation of FIR–submillimetre surveys that have and will conduct deep extragalactic surveys at 250–500 μm. With the peak in dust-obscured star-forming activity leading to present-day giant ellipticals now believed to occur in submillimetre galaxies near $z \sim 2.5$, these new FIR–submillimetre surveys will directly sample the spectral energy distributions of these distant objects at rest-frame FIR wavelengths similar to those at which local galaxies were observed by *IRAS*. We have taken care to correct for the temperature bias and the evolution effects in our *IRAS* 60-μm-selected sample. We verify that our colour–luminosity distribution is consistent with the measurements of the local FIR luminosity function, before applying it to the higher redshift Universe. We compare our colour–luminosity correlation with recent dust–temperature measurements of submillimetre galaxies and find evidence for pure luminosity evolution of the form $(1 + z)^3$. This distribution will be useful for the development of evolutionary models for Balloon-borne Large Aperture Submillimeter Telescope (BLAST) and Spectral and Photometric Imaging Receiver (SPIRE) surveys as it provides a statistical distribution of the rest-frame dust temperatures for galaxies as a function of luminosity.

Key words: galaxies: evolution – galaxies: high-redshift – galaxies: luminosity function, mass function – infrared: galaxies – submillimetre.

1 INTRODUCTION

Deep extragalactic surveys at submillimetre wavelengths (∼200–1200 μm) over the last 10 years have uncovered a population of luminous infrared galaxies ($L > 10^{12}\,L_\odot$) with star formation rates inferred to be ≫1000 $M_\odot\,yr^{-1}$ (e.g. Smail, Ivison & Blain 1997; Barger et al. 1998; Hughes et al. 1998; Eales et al. 1999; Cowie, Barger and Kneib 2002; Scott et al. 2002; Borys et al. 2003; Serjeant et al. 2003; Webb et al. 2003; Greve et al. 2004; Wang, Cowie and Barger 2004; Coppin et al. 2005; Laurent et al. 2005; Coppin et al. 2006; Knudsen et al. 2006; Bertoldi et al. 2007; Greve et al. 2008; Perera et al. 2008; Scott et al. 2008). These submillimetre galaxies (SMGs) are believed to be high-redshift ($z > 1$) analogues, and in many cases more luminous examples, of local ultra-luminous infrared galaxies (ULIRGs) discovered with *IRAS* 20 years ago (Sanders & Mirabel 1996). Furthermore, the rest-frame wavelengths sampled by submillimetre surveys of the highest redshift SMGs approach those of the far-infrared (FIR) *IRAS* observations. Appearing in vast quantities consistent with the massive evolution of the local ULIRG population, these SMGs are now believed to represent an important early stage in the evolutionary sequence that ultimately

produce locally observed massive elliptical galaxies (e.g. Scott et al. 2002; Blain et al. 2004). Thus, to this day, the local FIR luminosity function measured by *IRAS* continues to be useful for interpreting the results of these longer wavelength surveys.

Additional motivation for studying the *IRAS* luminosity function, and its connection with the higher redshift SMG population, comes from the shape and the magnitude of the cosmic infrared background (CIB) measured by *COBE* which peaks near 200 μm (e.g. Fixsen et al. 1998). Its broad shape resembles the superposition of many thermal spectral energy distributions (SEDs), which can be interpreted as evidence for a population of sources at redshifts $z < 1$ with a large range of physical temperatures, or alternatively, as a population with a narrower range of temperatures, but residing over a greater range of redshifts, including a significant fraction at $z > 1$ (the SMG population). This latter possibility is supported by the fact that the total energy density of the CIB (Franceschini et al. 2001) exceeds the contribution of local *IRAS* galaxies by a factor of ∼3 (Soifer & Neugebauer 1991).

In this paper, we examine the colour–luminosity correlation and luminosity function of *IRAS* galaxies, which together are an important reference for constraining models of galaxy evolution with a new generation of submillimetre surveys at shorter wavelengths. It has been known for some time that more luminous *IRAS* galaxies exhibit warmer dust temperatures (e.g. Soifer &

★E-mail: echapin@phas.ubc.ca

Neugebauer 1991). This relationship is important for a class of phenomenological models (e.g. Blain & Longair 1993; Guiderdoni et al. 1997; Blain et al. 1999; Chary & Elbaz 2001; Malkan & Stecker 2001; Rowan-Robinson 2001; Lagache, Dole & Puget 2003; Lagache et al. 2004) that have been used to predict the source counts and redshift distributions at FIR wavelengths for the *Spitzer Space Telescope* (Werner et al. 2004) and *Akari* (Matsuhara et al. 2006) and at submillimetre wavelengths, for instruments such as Submillimetre Common-User Bolometer Array (SCUBA; Holland et al. 1999), Max-Planck Millimeter Bolometer Array (MAMBO) (Kreysa et al. 2002), Large Apex Bolometer Camera (LABOCA) (Kreysa et al. 2003), *Herschel*/SPIRE (Griffin et al. 2006), SCUBA-2 (Holland et al. 2006), Aztronomical Thermal Emission Camera (AzTEC) (Wilson et al. 2008) and BLAST (Pascale et al. 2008). These models often use the shape of the CIB as an integral constraint, since the total surface brightness of galaxies at each wavelength cannot exceed the measured diffuse background. These authors apply evolution to the local luminosity functions to obtain estimates of the redshift-dependent luminosity function $\Phi(L, z)$. In order to compare these models with observations, SED templates are adopted to extrapolate observed flux densities from the rest-frame luminosities. In a number of cases, it has been beneficial to fit data over a range of wavelengths by dividing the local luminosity function into several discrete populations, each with different SED templates and separate evolutionary forms (e.g. Blain et al. 1999; Rowan-Robinson 2001; Lagache et al. 2003, 2004). Recently, Wall, Pope & Scott (2008) demonstrated direct evidence for the presence of at least two significant populations in a sample of submillimetre luminous sources in Great Observatories Origins Deep Survey-North (GOODS-N). The luminosity–colour correlation can be useful for such models as a method for assigning dust temperatures to SED templates as a function of luminosity. For example, Lagache et al. (2003) use the observed *IRAS* colour–luminosity distribution of Soifer & Neugebauer (1991), and Lewis, Chapman & Helou (2005) use the FIR colour–luminosity distribution of Chapman et al. (2003, hereafter C03) inferred from a model fit to *IRAS* data.

C03 calculate $\Phi(L, C)$, the galaxy volume density as a function of total 3–1100 μm luminosity, L_T and the 60–100 μm colour, $C \equiv \log(S_{60}/S_{100})$. They formulate $\Phi(L, C)$ as the product of a luminosity function and the distribution in C as a function of L. The two functions are fit independently, with the latter being constrained directly from the observed distribution of the ratio of broad-band *IRAS* 60 and 100 μm fluxes.

In this work, we provide a more accurate measurement of the joint colour–luminosity distribution using a single maximum-likelihood optimization to solve for all of the model parameters simultaneously. Our methodology also differs from that of C03 in several other key respects: (i) rather than calculating C with observed *IRAS* broad-band fluxes we use rest-frame monochromatic 60 and 100 μm flux densities derived from fitted SEDs, (ii) we use narrower bandwidth 42.5–122.5 μm FIR luminosities instead of 3–1100 μm total infrared (TIR) luminosities to minimize the dependence of the fitted distribution on the choice of SED templates, (iii) a correction for redshift evolution in the *IRAS* galaxy population is applied and (iv) we account for a bias against the detection of cooler sources caused by the 60 μm selection criterion for the sample. Our galaxy sample, SED fitting procedure and methods for calculating luminosities and volumes are described in Section 2. The luminosity function and colour–luminosity distribution are calculated in Section 3. We discuss the choice of luminosity variable, and its consequences, in Section 4.1. Finally, we compare the local colour–luminosity

correlation with the observed values for high-redshift SMGs in Section 4.2 and test a simple evolutionary model. Throughout this paper a standard cosmology is adopted with $\Omega_M = 0.23$, $\Omega_\Lambda = 0.77$ and $H_0 = 74\,\mathrm{km\,s^{-1}\,Mpc^{-1}}$.

2 SAMPLE PREPARATION

We use the same flux-limited $S_{60} > 1.2\,\mathrm{Jy}$ *IRAS* sample of Fisher et al. (1995) as in C03. Their catalogue covers most of the sky and provides 60 and 100 μm flux densities as well as spectroscopic redshifts for each galaxy. The cool, high-luminosity region of the observed colour–luminosity plane found to contain a large number of spurious sources in C03 has also been excised. We use this sample to first calculate a non-parametric (binned) FIR luminosity function and then fit it with simple parametric models.

2.1 SEDs, luminosities and colours

To calculate rest-frame luminosities and colours from observed *IRAS* 60 and 100 μm flux densities, we follow the method of Saunders et al. (1990). A single temperature-modified blackbody SED is assumed for each source, $S(\nu) = A\,\nu^\beta B_\nu(T_{obs})$. The dust emissivity index is fixed at $\beta = 1.5$ which is consistent with the typical values measured for local ULIRGs with submillimetre follow-up (e.g. Dunne et al. 2000; Klaas et al. 2001; Yang & Phillips 2007). All of the subsequent analysis in this paper has also been repeated using values $\beta = 1.0$ and 2.0, and the variation in the results is well within the quoted uncertainties. The remaining two parameters, the amplitude A and the observed temperature T_{obs}, are then uniquely determined from the observed S_{60} and S_{100}. For this fit, we take into account the broad *IRAS* passbands (Beichman et al. 1988). Bolometric luminosities are calculated by integrating the fitted SED directly – the bolometric flux emitted in the rest-frame, S_{bol} is simply the integral of the observed SED across the redshifted band, $S_{bol} = \int_{c/\lambda_u(1+z)}^{c/\lambda_l(1+z)} S(\nu)d\nu$, where $\lambda_l = 122.5\,\mu m$ and $\lambda_u = 42.5$,μm for FIR fluxes, and $\lambda_l = 1100\,\mu m$ and $\lambda_u = 3\,\mu m$ for TIR fluxes. Similarly, the colour C is calculated from the logarithm of the ratio of monochromatic flux densities emitted at 60 and 100 μm in the rest-frame by the model SED.

Rather than a simple modified blackbody, C03 adopt the range of model SED templates from Dale et al. (2001). This difference has a negligible effect on the inferred FIR luminosities since there is very little structure in the Dale et al. (2001) SEDs at 42.5–122.5 μm that is not characterized by the single temperature variable in our SED model (despite the correlation between luminosity and β assumed in Dale et al. 2001). For example, assuming temperatures ranging from 30 to 50 K (and $\beta = 1.5$), the FIR luminosities inferred from our modified blackbody templates as compared to the Dale et al. (2001) SEDs with the same corresponding values of C agree to within ∼5 per cent. Since the difference is so small, and for the sake of simplicity, we therefore proceed with the modified blackbody SED model to measure the FIR colour–luminosity distribution. The TIR luminosity, however, cannot be estimated from the modified blackbody model as there is significant emission in the mid-infrared (MIR) spectrum (∼3–60 μm) that is missed by the steep drop on the Wien side (e.g. Blain, Barnard & Chapman 2003, and discussion in Section 4.1). Our modified blackbody SEDs in this temperature range underpredict the TIR luminosities obtained from the Dale et al. (2001) SEDs by about 30 per cent. We only use their templates to calculate TIR luminosities that are consistent with C03 for the discussion in this section (Fig. 1) and Section 3.1 (Fig. 3).

Another fundamental difference between this work and C03 is the definition of FIR colour. Whereas we choose to define C in
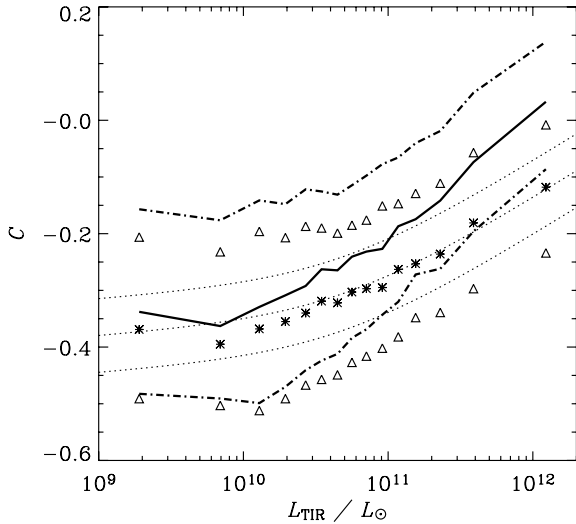
Figure 1. Observed *IRAS* FIR colour distribution [$C \equiv \log(S_{60}/S_{100})$] as a function of 3–1100 μm TIR luminosity. Stars and triangles show the mean and 68 per cent confidence intervals when C is calculated from broad-band *IRAS* fluxes following the prescription in C03. The dotted lines show the mean and 1σ envelope of the fitted C03 colour–luminosity correlation for reference. The thick solid and dot-dashed lines show the mean and 68 per cent confidence intervals of the distribution when C is calculated with monochromatic flux densities emitted at 60 and 100 μm in the rest-frame.

terms of the ratio of rest-frame monochromatic flux densities, C03 use observed broad-band *IRAS* fluxes. We believe our definition is more useful as a general reference since no detailed knowledge of the *IRAS* passbands is required in order to use our colour–luminosity distribution. Furthermore, we find that the strength of the colour–luminosity correlation is relatively diluted when using broad-band fluxes. In Fig. 1, we show the distribution of *IRAS* galaxy colours as a function of TIR luminosity derived from fits of the Dale et al. (2001) SED templates. The stars and triangles correspond to the mean and 68 per cent confidence intervals using observed broad-band *IRAS* fluxes, effectively reproducing the top panel of fig. 1 in C03. The thick solid line and dot-dashed lines show the mean and 68 per cent confidence interval of the colour distribution using the ratio of monochromatic 60 and 100 μm flux densities emitted in the rest-frame. At luminosities $L \lesssim 10^{10}\,L_{\odot}$, there is little difference in the shapes of the distributions. At $L \gtrsim 10^{10}\,L_{\odot}$, however, the colour–luminosity correlation is significantly steeper.

The dotted lines in Fig. 1 show the mean and 1σ envelope of the C03 colour–luminosity correlation. We note that although the mean of this fitted parametric distribution clearly tracks the stars in the plot, the standard deviation of the distribution, $\sigma_C = 0.065$, appears to have been underestimated. We find that both the 68 per cent confidence intervals and the standard deviations of C, for each luminosity bin, are typically closer to 0.13.

2.2 Evolution in the sample

Since the most distant, luminous objects in *IRAS* samples exhibit the effects of strong luminosity and/or density evolution (e.g. Saunders et al. 1990; Kim & Sanders 1998; Lawrence et al. 1999), we must account for its effect in our measurement of the local luminosity function. Rather than fitting for this evolutionary form ourselves, we instead apply an explicit correction based on the luminosity evolutionary form fit by Saunders et al. (1990): the luminosity of

each galaxy is divided by a factor of $(1 + z)^3$ corresponding to its redshift. We have chosen to apply a luminosity, rather than a density evolution correction for consistency with the discussion in Section 4.2.

2.3 Accessible volumes

The $\sum(1/V_{max})$ estimator (Schmidt 1968) with accessible volumes V_{max} corresponding to the largest redshift at which a galaxy would be detected given the survey flux limit, used in C03, is appropriate for the monochromatic 60 μm luminosity function. In this case, a given object's luminosity, L_{60}, is a function of the observed flux density and distance only. Therefore, the maximum volume in which the given object can be detected corresponds to the distance at which the observed S_{60}, given its L_{60}, drops below the flux limit of the sample. For the broad-band FIR luminosity function described here, however, the relationship between L_F and S_{60} is more complicated and this simple method is invalid. There exists a bias against the detection of cooler sources given the shape of the galaxy SEDs (Saunders et al. 1990). The wavelength of the peak FIR emission is typically in the range 60–200 μm. The SEDs of warmer objects peak closer to 60 μm, and colder objects at longer wavelengths, so that, in general, for a fixed 60 μm flux density a colder object must be *more FIR luminous* to be included in the sample.

Saunders et al. (1990) derive the FIR luminosity function from their 60 μm flux-limited survey by selecting a subsample of objects brighter than a FIR flux limit that corresponds to their 60 μm flux limit *and* the coolest dust temperature that they observed, 23 K (see section 6.5 in Saunders et al. 1990). However, this selection reduces the size of their sample from ∼3000 objects to 1004. There is also an underlying assumption that there is no significant population of sources with dust temperatures $T < 23$ K.

In this work, we use the entire sample, but calculate accessible volumes using a modified formalism that accounts for the dependence of L_F on the FIR colour. Given an observed temperature T_{obs} and redshift z, the rest-frame temperature T and the total luminosity for an object are calculated. The accessible volume corresponds to the maximum redshift at which an object with its rest-frame luminosity *and* temperature would be detected in the sample, or correspondingly the distance at which its observed flux density in the *IRAS* 60μm passband is 1.2 Jy.

3 THE Φ(*L, C*) DISTRIBUTION

3.1 Non-parametric (binned) estimate

With luminosities and accessible volumes for all of the objects in the sample, we first calculate the non-parametric (binned) colour–luminosity distribution, $\Phi_b(L, C)$. Since the accessible volume is now parametrized by both L and C, the modified $\sum(1/V_{max})$ estimator is simply

$$\Phi_b(L, C)\mathrm{d}L\mathrm{d}C = \frac{4\pi}{\Omega_s}\sum_i \frac{1}{V_i}, \qquad (1)$$

where $\Phi_b(L, C)\,\mathrm{d}L\mathrm{d}C$ is the number of sources in the area of the L–C plane, and the sum runs over all of the galaxies, i, with luminosity–evolution-corrected luminosities (Section 2.2) and colours that land within the bin, and with accessible volumes V_i. The factor in front of the sum is the fraction of the sky covered by the survey. The binned luminosity function may be derived from this distribution by marginalizing over C,

$$\Phi_b(L)\mathrm{d}L = \sum_j \Phi_b(L, C)\mathrm{d}L\mathrm{d}C, \qquad (2)$$
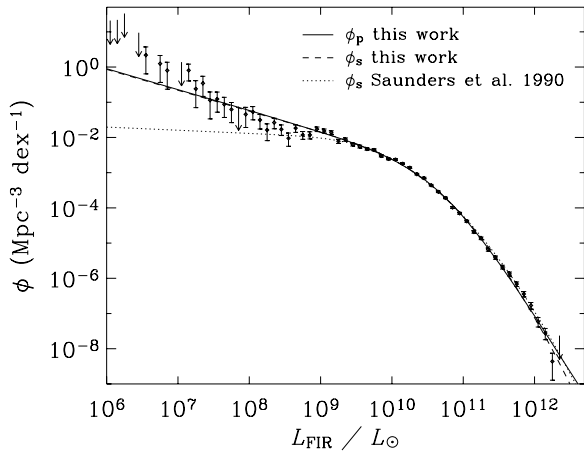
Figure 2. The non-parametric 42.5–122.5 µm FIR luminosity function (symbols with 68 per cent Poisson error bars and arrows show 95 per cent upper limits for bins with <2 objects) and two parametric fits (equation 6 as a solid line and equation 7 as a dashed line) derived from the $S_{60} > 1.2$ Jy *IRAS* sample of Fisher et al. (1995). The parametric FIR luminosity function of Saunders et al. (1990) is shown for comparison as a dotted line.

Figure 3. The non-parametric 3–1000 µm TIR luminosity function (symbols with 68 per cent Poisson error bars and arrows show 95 per cent upper limits for bins with <2 objects) and the parametric fit of C03 (solid line). The discrepancies at $L > 10^9 \, L_\odot$ are due to the corrections described in Sections 2.2 and 2.3.

where j runs over all of the bins along the C axis. We define a second representation of the luminosity function using a lowercase ϕ,
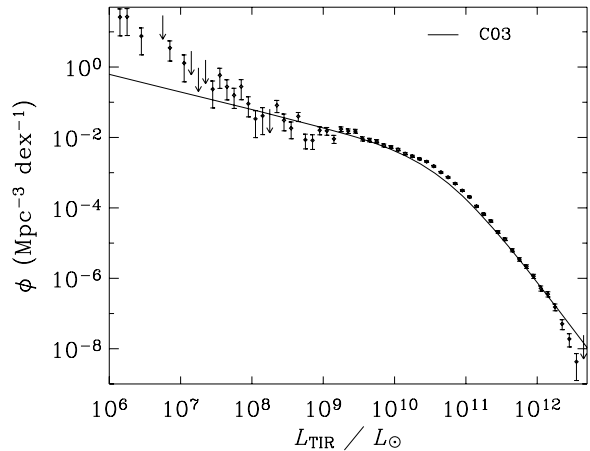
$$\phi(L) = \ln(10) L \Phi(L), \tag{3}$$

which changes the units from $\mathrm{Mpc}^{-3} \, L_\odot^{-1}$ to the more typical $\mathrm{Mpc}^{-3} \, \mathrm{dex}^{-1}$, in order to assist comparison with other work. This representation of our FIR luminosity function is shown in Fig. 2.

At luminosities $L \gtrsim 10^9 \, L_\odot$, there is an excellent agreement between our luminosity function and the measurement of Saunders et al. (1990) (shown in Fig. 2 with a dotted line). However, at fainter luminosities our luminosity function includes many more objects. The reason for this discrepancy is probably due to our choice of $\sum(1/V_{\max})$ estimator, and the fact that over this luminosity range the sample is dominated by an overdensity of galaxies in the local supercluster. It is for this reason that Saunders et al. (1990) used an alternative estimator that is insensitive to the local density variations. Their method has the potential to more accurately determine the *shape* of the luminosity function, however, at the expense of losing the absolute normalization. At luminosities $L \gtrsim 10^9 \, L_\odot$, the galaxies are typically sufficiently distant that this issue is no longer important, and both estimators give consistent answers (see section 8 of Lawrence et al. 1999). In addition to this effect, Yun, Reddy & Condon (2001) suggest that some of the flattening at faint luminosities in the Saunders et al. (1990) luminosity function may be due to the sample incompleteness.

We also produce the non-parametric TIR luminosity function for comparison with the parametric form of C03 in Fig. 3. For this calculation, we have used the same Dale et al. (2001) SED templates as C03 to derive TIR luminosities. The C03 model[1] has a significantly different shape as compared to our binned representation at luminosities $L > 10^9 \, L_\odot$, the range over which the local overdensity of galaxies is irrelevant. Their model underpredicts the binned

luminosity function by a factor of ∼30 per cent at $5 \times 10^{10} \, L_\odot$, and rises to overpredict by a similar factor at $2 \times 10^{12} \, L_\odot$. We have determined that this discrepancy can be explained entirely by the effects described in Sections 2.2 and 2.3, since the model and the bins are otherwise consistent without them. Applying only the correction for evolution in the sample, we find that the number of objects in the brightest bins decreases – explaining the factor of 30 per cent at luminosities $>10^{12} \, L_\odot$. The reason for this is that these objects are the most distant, and therefore exhibit the strongest effects of redshift evolution. This correction has almost no effect by $10^{11} \, L_\odot$. In contrast, applying the correction for accessible volumes increases the numbers of objects in bins at luminosities primarily $\lesssim 10^{11} \, L_\odot$. This increase is caused by the fact that less luminous objects are cooler, with correspondingly smaller volumes in which they could be detected given the 60 µm flux limit. Together, these corrections demonstrate that the luminosity function is in fact significantly steeper than the result of C03 at luminosities $\gtrsim 10^{10} \, L_\odot$, the most important range for comparison with results from new submillimetre surveys of distant star-forming galaxies.

3.2 Maximum-likelihood model fits

Next, we fit simple parametric models to the data by maximizing the likelihood of observing the sample. For the remainder of this paper, we consider only FIR luminosities to avoid dependence on assumptions about the shape of the MIR SED (Section 4.1). At a given position in the L–C plane, the expected number of sources from our sample to have landed in that bin, given a model for $\Phi(L, C)$, is

$$\mu(L, C) = V_{\max} \frac{\Omega_s}{4\pi} \Phi(L, C) \mathrm{d}L \mathrm{d}C. \tag{4}$$

These expectations are used to calculate the joint Poisson likelihood of the data.

We express the model, $\Phi(L, C)$, as the product of the luminosity function, $\Phi(L)$, and the conditional probability of a galaxy having a colour C given the luminosity L, $p(C|L)$,

$$\Phi(L, C) = \Phi(L) p(C|L). \tag{5}$$

---

[1] We take the luminosity function to be $\sigma_C (2\pi)^{1/2} \Phi_1(L)$ from section 3.2 in C03. The dimensionless pre-factor is needed since their colour distribution, $\Phi_2(C)$, is an unnormalized Gaussian with standard deviation σ_C. Also, we have assumed that the units for ρ_* are $\mathrm{Mpc}^{-3} \, \mathrm{dex}^{-1}$ rather than $\mathrm{Mpc}^{-3} \, L_\odot^{-1}$ as indicated.

3.2.1 Parametric forms of $\Phi(L)$

For $\Phi(L)$, we consider two forms. The first is the dual power law of C03,

$$\Phi_p(L) = \rho_* \left(\frac{L}{L_*}\right)^{(1-\alpha)} \left(1 + \frac{L}{L_*}\right)^{-\beta}, \qquad (6)$$

where L_* is the characteristic knee luminosity, ρ_* is the number density normalization of the function at L_* (Mpc^{-3} L$_\odot^{-1}$) and α and β characterize the power laws at the faint ($L < L_*$) and bright ($L > L_*$) ends, respectively, of the luminosity function.

The other form considered is the hybrid power-law/Gaussian form preferred by Saunders et al. (1990),

$$\Phi_s(L) = \rho_* \left(\frac{L}{L_*}\right)^{(1-\alpha)} \exp\left[-\frac{1}{2\sigma^2} \log_{10}^2\left(1 + \frac{L}{L_*}\right)\right] \times \frac{1}{\ln(10)L}. \qquad (7)$$

Maximum-likelihood solutions for both forms are shown in Fig. 2. At the faint end ($L_{\text{FIR}} < L_*$), both functions approach power laws, and are therefore indistinguishable. At the extreme bright end, they diverge; ϕ_s curves below ϕ_p at $L \sim 10^{12}$ L$_\odot$, although both forms lie mostly within the error bars of the non-parametric estimate.

To characterize the quality of the fits, we calculate values of reduced χ^2 for luminosity bins that contain at least 10 objects, approximately luminosities 5×10^8–10^{12} L$_\odot$ (with this number of objects, the Poisson error distribution is reasonably approximated by a Gaussian). Over this range, the power-law form produces a value of reduced $\chi^2 = 2.2$ and the hybrid form 2.4. Given the similarity of these values, and the fact that each form has the same number of parameters, we feel that there is no compelling evidence to favour one model over the other given the data. While the choice has no impact on the subsequent discussion in this paper, we note that the two forms rapidly diverge at luminosities $> 10^{12}$ L$_\odot$, potentially the most important region of the luminosity function for comparison with the results of submillimetre surveys. For example, while at 10^{12} L$_\odot$ the power law only exceeds the Saunders et al. (1990) form by about 10 per cent, at 10^{13} L$_\odot$, it is nearly an order of magnitude larger. Fitted parameters for both models are given in Appendix A, and they should only be considered valid to a maximum luminosity of $\sim 2 \times 10^{12}$ L$_\odot$.

3.2.2 Parametric form of $p(C|L)$

In C03, it was shown that the distribution in C is approximately Gaussian at a particular value of L. The precise functional form we have adopted is
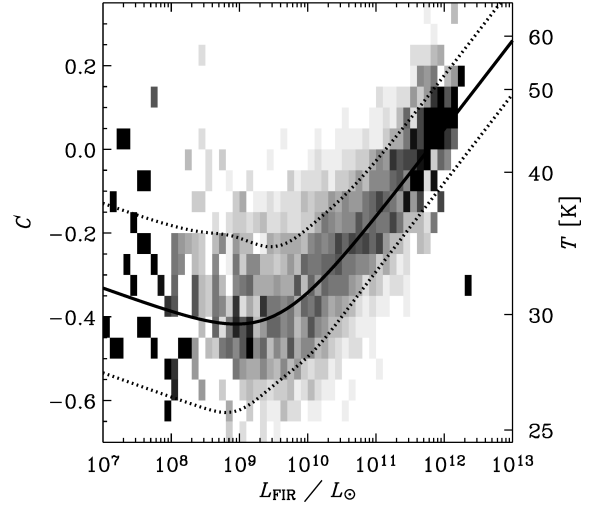
$$p(C|L) = \frac{1}{\sigma_C \sqrt{2\pi}} \exp\left[-\frac{1}{2} \times \left(\frac{C - C_0}{\sigma_C}\right)^2\right], \qquad (8)$$

with the mean colour at a given luminosity given by[2]

$$C_0 = C_* - \delta \log_{10}\left(1 + \frac{L'}{L}\right) + \gamma \log_{10}\left(1 + \frac{L}{L'}\right). \qquad (9)$$

Note that unlike C03, the 'knee' luminosity, L', for $p(C|L)$ is independent of the knee luminosity for the luminosity function, L_*. In

---

[2] We note that in section 3.2 of C03, the expression for C_0 is clearly meant to be the logarithm of the third equation in Section 3.1 – the form we have adopted here.


Figure 4. Comparison between parametric (solid and dotted lines give the mean and 1σ envelope of equation (8), respectively) and non-parametric estimates of $p(C|L)$ (grey-scale shows $\Phi_b(L, C)$ normalized along the C axis). The temperature axis is derived from C assuming a dust emissivity index $\beta = 1.5$. At luminosities $L \lesssim 10^8$ and $L \gtrsim 10^{12}$, the sample does not contain enough galaxies to accurately constrain the shape, and $p(C, L)$ is simply extrapolated in the parametric model.

addition, the width of the colour distribution, σ_c, is characterized by two different values: σ_f and σ_b at the faint and bright ends, respectively, with a smooth transition at L',

$$\sigma_c = \sigma_f(1 - 2^{-L'/L}) + \sigma_b(1 - 2^{-L/L'}). \qquad (10)$$

Fig. 4 compares the mean and 1σ envelope of the parametric $p(C|L)$ with a non-parametric estimate created by factoring the smooth model $\Phi(L)$ from the binned $\Phi_b(L, C)$.

It is argued in C03 that the width of the distribution in C is constant as a function of luminosity. The top panel of fig. 2 in C03 demonstrates a constant width in S_{60}/S_{100} with a logarithmic axis, in contrast with the bottom panel in which the width of the distribution is shown to broaden at greater luminosities when plotted with a linear axis. This behaviour motivates the definition $C \equiv \log(S_{60}/S_{100})$. However, this plot appears to be at odds with the top panel of fig. 4 in C03 which exhibits a systematic broadening at higher luminosities. Such a trend does not appear to be present in our measurement of $p(C|L)$. For clarity, we compare slices of the parametric estimate of $p(C|L)$ at several fixed luminosities with the binned estimate in Fig. 5. The good agreement between these two estimates, both in terms of scatter and systematic variations, indicates that equation (8) adequately describes the shape of $p(C|L)$. We find that the width of the distribution narrows with increasing brightness to $\sigma_b = 0.13$ from $\sigma_f = 0.2$ at a transition luminosity of $\sim 3.5 \times 10^9$ L$_\odot$ (Appendix A). The broadening shown in C03 at greater luminosities does not appear to be caused by their choice of SEDs or of broad-band over monochromatic colours. The most likely explanation is an artefact of the C03 griding scheme. They use variable-width luminosity bins which contain equal numbers of objects, in contrast to our method which uses equally spaced logarithmic bins. The wide, sparsely populated high-luminosity bins may simply dilute the colour–luminosity correlation. We note that our fitted value for σ_b appears to be consistent with the width of the distribution in the lowest, narrowest, luminosity bins in the top panel of fig. 4 from C03 (although they claim a smaller standard deviation
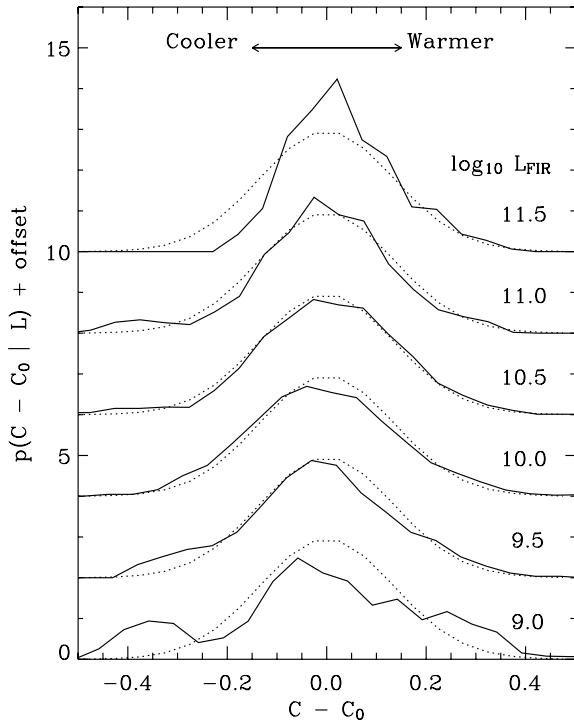
Figure 5. The distribution of FIR colours, C, about the mean, C_0 (equation 9), at a range of luminosities. The solid lines are normalized slices of the measured (non-parametric) $p(C|L)$ $[\Phi_b(L, C)/\Phi_b(L)$ – see equations 1 and 5] evaluated at $C - C_0$, and numbers indicate $\log_{10}(L_{FIR})$. The parametric model (equation 8) is shown as a dotted line.

of 0.065; see Fig. 1 and the discussion at the end of Section 2.1 in this paper).

3.2.3 Parameter uncertainties

We characterize the uncertainties in the 10 parameters of $\Phi(L, C)$, for both parametric forms of $\Phi(L)$, using a bootstrap Monte Carlo technique. First, 100 realizations of the 1.2 Jy survey are created from the actual survey data by randomly sampling sources from the catalogue with replacement (see section 6.6 of Wall & Jenkins 2003). We then fit the model to each simulated sample. From these 100 fits, we calculate the sample variances and the covariances between all pairs of parameters to estimate the full parameter covariance matrix. The maximum-likelihood values of each parameter, their standard deviations and the Pearson correlation matrices are given in Appendix A. Note that the parameters for $p(C|L)$ are largely independent of the parametric form chosen for $\Phi(L)$.

4 DISCUSSION

4.1 Choice of bolometric luminosity variable

In this work, we have chosen to use the 42.5–122.5 μm FIR luminosity instead of the wider-bandwidth 3–1100 μm TIR luminosity, L_T, as in C03. An argument for using the latter is that it includes a significant fraction of the total power emitted by a galaxy that is missed at shorter wavelengths (<40 μm) – an effect which becomes increasingly important at high luminosities given the positive L–C correlation. By using L_{FIR}, the 'clipping' of shorter wavelength light

obscures the physical interpretation of the correlation between the two variables.

Our primary goal, however, is to assist with the development of a model for the luminosity function of SMGs discovered in BLAST (Pascale et al. 2008) and future *Herschel*/SPIRE (Griffin et al. 2006) 250–500 μm surveys, as well as any other surveys at similar wavelengths. It is now generally accepted that the redshift distribution for the bulk of SMGs discovered in 850 μm SCUBA surveys peaks at redshifts ~2.5. For example, the radio-detected spectroscopic sample of C03 and Chapman et al. (2005) finds a median redshift of 2.2 with an interquartile range of $z = 1.7$–2.8, in general agreement with several other studies using radio–FIR or radio and 24 μm-guided photometric redshift estimates (e.g. Aretxaga et al. 2003, 2007; Pope et al. 2006). Since the negative K-correction produces a nearly unbiased detection efficiency at 850 μm for a typical ULIRG SED at $z \sim 1$–8 (e.g. Blain et al. 2002), the observed redshift distribution is a reasonable proxy for the total dust-obscured star formation rate history of massive galaxies. If SMGs have thermal SEDs similar to the ULIRGs that populate the bright end of the *IRAS* luminosity function presented here, their SEDs peak at wavelengths ~60–200 μm in the rest-frame, and they are redshifted into the 200-600 μm BLAST and SPIRE bandpasses near the peak of their redshift distribution.

As an example, Fig. 6 shows the SED of the ULIRG Arp 220 at a redshift $z = 2.5$ as compared to the BLAST and SPIRE bandpass region and the integrated FIR and TIR fluxes. Clearly, the BLAST and SPIRE-integrated fluxes match the rest-frame FIR flux more closely than the TIR flux.
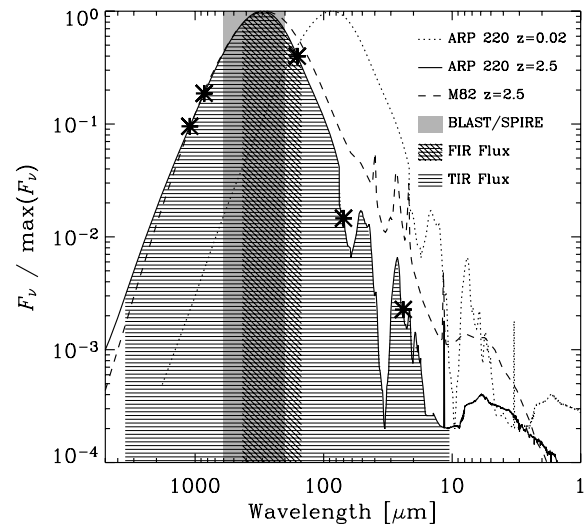
Figure 6. The peak-normalized SED of Arp 220 (dotted line) and shifted to $z = 2.5$ (solid line). The complete observed BLAST and SPIRE band (200–600 μm, including the 30 per cent finite bandpasses for each channel) is indicated by the solid grey-shaded rectangle. The rest-frame 3–1100 μm TIR flux and 42.5–122.5 μm FIR flux correspond to the integrals of the horizontal-line filled and cross-hatch filled regions, respectively, for the $z = 2.5$ SED. Clearly for objects at this redshift, the BLAST and SPIRE filters match the rest-frame FIR flux more closely than the TIR flux. The peak-normalized M82 SED redshifted to $z = 2.5$ (shown as a dashed line) illustrates the relatively large variations in the rest-frame MIR spectrum (~3–60 μm observed wavelength). Symbols indicate the wavelengths accessible from ground-based submillimetre surveys (e.g. SCUBA at 850 μm and AzTEC/MAMBO at 1.1mm), and existing space-based FIR data (e.g. *Spitzer* at 24, 70 and 160 μm), demonstrating their inability to accurately constrain the bolometric FIR luminosity for these galaxies.

The peak-normalized SED of the starburst galaxy M82 redshifted to $z = 2.5$ is shown for comparison as a dashed line to illustrate the relatively large scatter at MIR wavelengths compared to the smooth thermal SED at longer wavelengths. The rest-frame MIR SEDs of these example galaxies exhibit prominent polycyclic aromatic hydrocarbon absorption and emission features (the $\sim$100–10 µm range of the observed SED; measurements for actual SCUBA-selected SMGs are given in Pope et al. 2008). For these two examples there is a difference of $\sim$30 per cent in the contribution of the MIR emission to the TIR luminosity. For these reasons, evolutionary models based on the FIR luminosity function are less dependent on the assumptions about the intrinsic near-IR to millimetre–wavelength SEDs of high-redshift galaxies than the TIR luminosity function, enabling cleaner comparison with new and future data from deep submillimetre cosmological surveys. We emphasize the fact that one is free to adopt any template library to infer flux densities at other wavelengths for objects drawn from our $\Phi(L, C)$ distribution provided that they have roughly thermal FIR spectra and span the relevant range of rest-frame FIR colours $-0.65 \lesssim C \lesssim 0.25$ (see, for example, the comparison in Section 2.1 between our modified blackbody SED model and the library of Dale et al. 2001).

4.2 Evidence for an evolving colour–luminosity correlation

Evolution in the FIR colour–luminosity distribution is difficult to probe from *IRAS* catalogues given their relatively low redshifts. For example, the median galaxy redshift in the Fisher et al. (1995) sample is $z = 0.019$, and the most distant object is at $z = 0.326$. Despite this, it has been possible to place weak constraints on the evolutionary form of the FIR luminosity function. Saunders et al. (1990) found that the most distant galaxies could undergo extremes of pure density evolution of the form $(1 + z)^{7 \pm 2}$, or pure luminosity evolution of the form $(1 + z)^{3 \pm 1}$ (we use this latter form explicitly to correct our sample, see Section 2.1). Since the most distant *IRAS* galaxies are also the brightest in the sample (luminosities $>L_*$), it is not possible to determine which form (or combination) is the more relevant.

At higher redshifts, the best constraints on the evolution of ULIRGs come from SCUBA surveys at 850 µm. It can be shown, for example, that continued luminosity evolution in the bright end of the local FIR luminosity function of the same form as Saunders et al. (1990) to redshifts $\sim$2–3 can be used to fit millimetre–submillimetre source counts, assuming ULIRG-like SEDs to extrapolate observed flux densities from rest-frame luminosities (e.g. Scott et al. 2002; Lagache et al. 2003). A more direct test of evolution for a small sample of SMGs with known redshifts was recently performed by Wall et al. (2008) finding similar results. Unfortunately, until recently, shorter wavelength data that would help to constrain the dust temperatures of objects in these samples are generally unavailable, and it is therefore not possible to search directly for *colour* evolution. Measuring dust temperatures for large samples ($\gg$1000) of SMGs is one of the primary science goals of BLAST and *Herschel*/SPIRE surveys – with the caveat that redshifts must first be determined independently for at least a subset of these new objects since there is a potential degeneracy between the apparent observed temperature and the redshift (e.g. Blain et al. 2003).

Recent Submillimeter High Angular Resolution Camera-II (SHARC-II) 350 µm observations of SMGs (e.g. Kovács et al. 2006; Coppin et al. 2008), however, have enabled improved estimates of dust temperatures for smaller samples (several tens of galaxies). In Fig. 7, 10 objects (triangles) with constrained dust temperatures and spectroscopic redshifts (median $z = 2.1$) from Coppin et al.
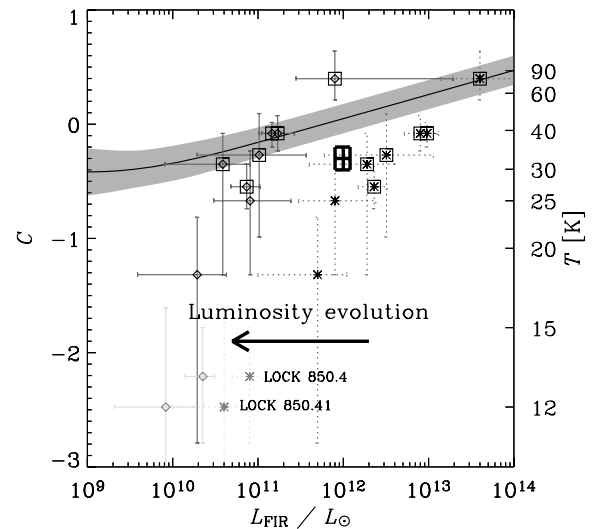
Figure 7. Comparison of local $p(C|L)$ (shaded region is the 68 per cent confidence interval, solid line is C_0 from equation 9) with data from Coppin et al. (2008). The temperature axis is derived from C assuming a dust emissivity index $\beta = 1.5$. Stars with dotted 1σ error bars indicate the 10 SMGs with spectroscopic redshifts and temperatures derived from observed 350/850 µm colours. Squares have been drawn around the symbols for the six objects at $z > 2$. High-redshift ultra-luminous galaxies appear systematically cooler than those in the local universe. Under the assumption of pure luminosity evolution of the form $(1 + z)^3$, the SMGs have been projected into the local colour–luminosity distribution by shifting them along the luminosity axis (diamonds with solid error bars). The model is a plausible fit to the data except for LOCK 850.4 and LOCK 850.41 which appear much cooler (shown as lighter symbols). These objects may have ambiguous or incorrect optical/IR counterpart identifications (discussed in Section 4.2). Future BLAST and SPIRE surveys will constrain FIR luminosities of $\sim$$10^{12}$ L$_\odot$ galaxies to $\sim$20 per cent, with uncertainties in C of $\sim$0.1 (several Kelvin). A representative measurement in the L–C plane is given by the thick cross-filled square.

(2008) are compared with our local measurement of $p(C|L)$. As noted in Kovács et al. (2006) and Coppin et al. (2008), the rest-frame temperatures for such luminous galaxies (median $L_{\mathrm{FIR}} = 2.3 \times 10^{12}$ L$_\odot$) are much lower than the objects in the local Universe. With the correlation between luminosity and FIR colour in-hand, we now ask the question: can pure luminosity evolution of the form $(1 + z)^3$ account for the apparently cooler temperatures of SMGs at high redshift? Explicitly, we express the redshift evolution of the FIR colour–luminosity distribution, $\Phi(L, C, z)$, as a simple function of the local distribution,

$$\Phi(L, C, z) = \Phi\left[\frac{L}{(1 + z)^3}, C\right]. \tag{11}$$

For comparison, we project each observed SMG into the local $p(C|L)$ distribution by dividing their luminosities by $(1 + z)^3$, shifting the objects to the left in Fig. 7 (diamonds). Given the uncertainties, the eight warmer objects (top of the plot) are roughly consistent with the local distribution once we apply this transformation. Ignoring the redshift uncertainties and adding the measured colour uncertainties, σ_{data}, in quadrature with the intrinsic colour width in the source population, σ_c (equation 10, at the evolution-corrected luminosity of the galaxy – the shaded region of the figure), we calculate residuals, R, between the model, C_0 (solid line through the

centre of the shaded region) and the measured colours, $C_{\rm data}$:

$$R = \frac{C_{\rm data} - C_0}{\sqrt{\sigma_{\rm data}^2 + \sigma_c^2}}. \tag{12}$$

We note that for five of these objects $R < 1$ and the remaining three are in the range $R = 1$–1.5; the approximate expectation for uncorrelated Gaussian uncertainties. This result is contrary to the conclusion of C03 who found that there was no need to invoke redshift evolution for $p(C|L)$ when comparing with lower redshift ($z < 1$) samples.

The two most significant outliers, LOCK 850.4 ($C = -2.2$, $z = 0.526$) and LOCK 850.41 ($C = -2.47, z = 0.689$), also the two coolest and least luminous objects, deserve further explanation. These two galaxies are also the only objects with redshifts $z < 1$. Since their observed submillimetre colours are otherwise similar to the other galaxies, these low redshifts also imply lower rest-frame dust temperatures (lower values of C). There is a possibility that the true optical counterpart (and hence redshift) for LOCK 850.4 is at $z = 1.482$, rather than 0.526 as adopted by Coppin et al. (2008). Both potential counterparts were proposed in Ivison et al. (2005). Adopting the higher redshift object as the counterpart, the inferred FIR luminosity increases from 8×10^{10} to 10^{12} L$_\odot$ and the rest-frame dust temperature from 13 to 21 K, or $C = -1$, at which point it would appear to have similar dust properties to the other galaxies in the sample. There is a similar possibility of a misidentification for LOCK 850.41. Two counterparts are suggested in Ivison et al. (2005), although they were only able to obtain the spectroscopic redshift indicated above for one of them. The other counterpart has an optical photometric redshift estimate of $z = 2.2 \pm 0.2$ from Dye et al. (2008). A similar value of $z = 2.1\pm_{0.6}^{1.4}$ based on its FIR colours is proposed in Aretxaga et al. (2007). Adopting a redshift of $z = 2.2$, the luminosity for LOCK 850.41 increases from 4×10^{10} to 5×10^{11} L$_\odot$ and the rest-frame dust temperature from 12 to 22 K, or $C = -0.9$, also closer to the distribution for the other objects in the sample. However, if the lower redshift candidates for these two galaxies are correct, and a population of galaxies with temperatures $T \lesssim 15$ K do exist in abundance at redshifts $z < 1$, it is possible that they were completely missed in the *IRAS* surveys, and will appear in the wide-area SCUBA-2, BLAST, and SPIRE surveys.

Finally, we note that the higher redshift objects generally fall closest to the colour–luminosity distribution. To emphasize this fact, we draw squares around the six objects in this small sample at redshifts $z > 2$. Naively this fact is slightly surprising, since one might suppose that the nearer objects are in fact more similar to the sample used to constrain the local distribution. However, an additional consideration is the selection function for this SCUBA sample. While the negative K-correction produces approximately the same observed 850 μm flux density at redshifts $z \sim 1$–8 for a fixed FIR luminosity and temperature, there is also a bias towards the detection of cooler objects at a fixed redshift and flux density since such objects are less luminous, and hence more abundant in the rest-frame (e.g. Eales et al. 1999; Blain et al. 2002; C03). For the lower redshift objects, at which point the negative K-correction is diminished, the luminosities are also fainter for a given flux density, and this bias could be increased due to the broadening in the colour–luminosity correlation that we have measured at lower luminosities.

This comparison is by no means an exhaustive study of evolution in the FIR colour–luminosity distribution. It is our goal to extend this investigation to much larger samples of SMGs with FIR colour information in new BLAST extragalactic surveys (Devlin et al. in preparation) and future *Herschel*/SPIRE surveys. Understanding the

details of this evolution is intimately related to the star formation rate history of massive galaxies, since the rest-frame FIR luminosity is the key-observed quantity in SMGs from which star formation rates are derived (e.g. Hughes et al. 1998; Kennicutt 1998; Scott et al. 2002; Pope et al. 2006).

5 CONCLUSIONS

We have measured the local FIR galaxy colour–luminosity distribution based on the 60 and 100 μm flux densities and redshifts from the Fisher et al. (1995) all-sky *IRAS* sample. This distribution is an important reference for the forthcoming BLAST and *Herschel*/SPIRE extragalactic surveys at 250, 350 and 500 μm that will detect thousands of SMGs at redshifts $z > 1$. Since the space density of SMGs appears to peak at redshifts $z \sim 2.5$, defining the epoch at which most of the stars in present-day massive galaxies formed, the BLAST and SPIRE bandpasses will sample the same region of the rest-frame SEDs for these objects as *IRAS* at 60 and 100 μm for local samples. Our measurement is therefore the primary present-day boundary condition with which any evolutionary model for the luminosity and dust–temperature distribution of SMGs must be compared. This applies to the current BLAST and the future SPIRE surveys, as well as higher resolution ground-based observations with SCUBA-2 for example.

Our method accounts for a temperature bias in the underlying 60 μm flux-limited sample, as well as luminosity evolution. These corrections indicate that the bright end of the luminosity function is significantly steeper than an earlier calculation by C03 which neglected them. We have verified that our distribution is consistent with the FIR luminosity function of Saunders et al. (1990) by marginalizing over colour. We fit a parametric model to the data consisting of the product of the luminosity function, $\Phi(L)$, with the conditional colour probability, $p(C|L)$, where $C \equiv \log(S_{60}/S_{100})$. We fit $p(C|L)$ using a normal distribution for C as a function of L, with a mean colour given by a broken logarithmic function also of L. This is characterized by the knee luminosity for the break, L', which is independent of the luminosity function knee, L_*, and the width of the distribution, by two different standard deviations $\sigma_{\rm b}$ and σ_f, above and below the knee L'.

We have directly checked for evolution in the colour–luminosity correlation using observations of high-redshift SMGs ($z > 1$) with temperatures constrained by SCUBA 850 μm and SHARC-II 350 μm photometry from Coppin et al. (2008). These high-z ultra-luminous objects appear much cooler than the local galaxies of comparable luminosities, and there is preliminary evidence that pure luminosity evolution in the local colour–luminosity distribution of the form $(1 + z)^3$ is consistent with the uncertainties in their measured redshifts and colours. This result is contrary to C03 who find no evidence for a change in the relationship between luminosity and colour in low-redshift ($z < 1$) samples.

REFERENCES

Aretxaga I., Hughes D. H., Chapin E. L., Gaztañaga E., Dunlop J. S., Ivison R. J., 2003, MNRAS, 342, 759

Aretxaga I. et al., 2007, MNRAS, 379, 1571

Barger A. J., Cowie L. L., Sanders D. B., Fulton E., Taniguchi Y., Sato Y., Kawara K., Okuda H., 1998, Nat, 394, 248

Beichman C. A., Neugebauer G., Habing H. J., Clegg P. E., Chester T. J., eds, 1988, Infrared Astronomical Satellite (IRAS) Catalogs and Atlases. Vol. 1: Explanatory Supplement, NASA, Washington DC

Bertoldi F. et al., 2007, ApJS, 172, 132

Blain A. W., Longair M. S., 1993, MNRAS, 264, 509

Blain A. W., Smail I., Ivison R. J., Kneib J.-P., 1999, MNRAS, 302, 632

Blain A. W., Smail I., Ivison R. J., Kneib J.-P., Frayer D. T., 2002, Phys. Rep., 369, 111

Blain A. W., Barnard V. E., Chapman S. C., 2003, MNRAS, 338, 733

Blain A. W., Chapman S. C., Smail I., Ivison R., 2004, ApJ, 611, 725

Borys C., Chapman S., Halpern M., Scott D., 2003, MNRAS, 344, 385

Chapman S. C., Helou G., Lewis G. F., Dale D. A., 2003, ApJ, 588, 186 (C03)

Chapman S. C., Blain A. W., Smail I., Ivison R. J., 2005, ApJ, 622, 772

Chary R., Elbaz D., 2001, ApJ, 556, 562

Coppin K., Halpern M., Scott D., Borys C., Chapman S., 2005, MNRAS, 357, 1022

Coppin K. et al., 2006, MNRAS, 372, 1621

Coppin K. et al., 2008, MNRAS, 384, 1597

Cowie L. L., Barger A. J., Kneib J.-P., 2002, AJ, 123, 2197

Dale D. A., Helou G., Contursi A., Silbermann N. A., Kolhatkar S., 2001, ApJ, 549, 215

Dunne L., Eales S., Edmunds M., Ivison R., Alexander P., Clements D. L., 2000, MNRAS, 315, 115

Dye S. et al., 2008, MNRAS, 386, 1107

Eales S., Lilly S., Gear W., Dunne L., Bond J. R., Hammer F., Le Fèvre O., Crampton D., 1999, ApJ, 515, 518

Fisher K. B., Huchra J. P., Strauss M. A., Davis M., Yahil A., Schlegel D., 1995, ApJS, 100, 69

Fixsen D. J., Dwek E., Mather J. C., Bennett C. L., Shafer R. A., 1998, ApJ, 508, 123

Franceschini A., Aussel H., Cesarsky C. J., Elbaz D., Fadda D., 2001, A&A, 378, 1

Greve T. R., Ivison R. J., Bertoldi F., Stevens J. A., Dunlop J. S., Lutz D., Carilli C. L., 2004, MNRAS, 354, 779

Greve T. R., Pope A., Scott D., Ivison R. J., Borys C., Conselice C. J., Bertoldi F., 2008, MNRAS, 389, 1489

Griffin M. et al., 2006, in Mather John C., MacEwen Howard A., de Graauw Mattheus W. M., eds, Proc. SPIE, Vol. 6265, Space Telescopes and Instrumentation I: Optical, Infrared, and Millimeter. Society of Photo-Optical Instrumentation Engineers (SPIE) Conf., Herschel-SPIRE: Design, Performance, and Scientific Capabilities. SPIE, Bellingham, p. 7

Guiderdoni B., Bouchet F. R., Puget J., Lagache G., Hivon E., 1997, Nat, 390, 257

Holland W. et al., 2006, in Zmuidzinas J., Holland W. S., Withington S., Duncan W. D., eds, Proc. SPIE Vol. 6275, Millimeter and Submillimeter Detectors and Instrumentation for Astronomy III. SPIE, Bellingham, p. 45

Holland W. S. et al., 1999, MNRAS, 303, 659

Hughes D. H. et al., 1998, Nat, 394, 241

Ivison R. J. et al., 2005, MNRAS, 364, 1025

Kennicutt R. C., Jr, 1998, ARA&A, 36, 189

Kim D.-C., Sanders D. B., 1998, ApJS, 119, 41

Klaas U. et al., 2001, A&A, 379, 823

Knudsen K. K. et al., 2006, MNRAS, 368, 487

Kovács A., Chapman S. C., Dowell C. D., Blain A. W., Ivison R. J., Smail I., Phillips T. G., 2006, ApJ, 650, 592

Kreysa E. et al., 2003, in Phillips T. G., Zmuidzinas J., eds, Proc. SPIE, Vol. 4855. SPIE, Bellingham, p. 41

Kreysa E., Gemünd H.-P., Raccanelli A., Reichertz L. A., Siringo G., 2002, in AIP Conf. Proc. 616, Experimental Cosmology at Millimetre Wavelengths Bolometer Arrays for Mm/Submm Astronomy. AIP, New York, p. 262–269

Lagache G., Dole H., Puget J.-L., 2003, MNRAS, 338, 555

Lagache G. et al., 2004, ApJS, 154, 112

Laurent G. T. et al., 2005, ApJ, 623, 742

Lawrence A. et al., 1999, MNRAS, 308, 897

Lewis G. F., Chapman S. C., Helou G., 2005, ApJ, 621, 32

Malkan M. A., Stecker F. W., 2001, ApJ, 555, 641

Matsuhara H. et al., 2006, PASJ, 58, 673

Pascale E. et al., 2008, ApJ, 681, 400

Perera T. A. et al., 2008, MNRAS, 391, 1228

Pope A. et al., 2006, MNRAS, 370, 1185

Pope A. et al., 2008, ApJ, 675, 1171

Rowan-Robinson M., 2001, ApJ, 549, 745

Sanders D. B., Mirabel I. F., 1996, ARA&A, 34, 749

Saunders W., Rowan-Robinson M., Lawrence A., Efstathiou G., Kaiser N., Ellis R. S., Frenk C. S., 1990, MNRAS, 242, 318

Schmidt M., 1968, ApJ, 151, 393

Scott S. E. et al., 2002, MNRAS, 331, 817

Scott K. S. et al., 2008, MNRAS, 385, 2225

Serjeant S. et al., 2003, MNRAS, 344, 887

Smail I., Ivison R. J., Blain A. W., 1997, ApJ, 490, L5

Soifer B. T., Neugebauer G., 1991, AJ, 101, 354

Wall J. V., Jenkins C. R., 2003, Practical Statistics for Astronomers. Princeton Series in Astrophysics. Cambridge University Press, Cambridge

Wall J. V., Pope A., Scott D., 2008, MNRAS, 383, 435

Wang W.-H., Cowie L. L., Barger A. J., 2004, ApJ, 613, 655

Webb T. M. et al., 2003, ApJ, 587, 41

Werner M. W. et al., 2004, ApJS, 154, 1

Wilson G. W. et al., 2008, MNRAS, 386, 807

Yang M., Phillips T., 2007, ApJ, 662, 284

Yun M. S., Reddy N. A., Condon J. J., 2001, ApJ, 554, 803

APPENDIX A: MODEL PARAMETERS AND UNCERTAINTIES

Maximum likelihood parameters and 1σ uncertainties for the local FIR colour-luminosity distribution are given in Tables A1 and A3. Pearson correlation coefficients for the uncertainties are given in Tables A2 and A4.

Table A1. Maximum-likelihood parameter values and 1σ uncertainties for $\Phi(L, C)$ (equation 5) using the C03 dual power-law form of the luminosity function [equation 6 and equations 8–10 for $p(C|L)$].

Parameter	Value
ρ_*	$(1.22 \pm 0.24) \times 10^{-14}$ Mpc^{-3} L$^{-1}_{\odot}$
α	2.59 ± 0.03
L_*	$(5.14 \pm 0.39) \times 10^{10}$ L$_{\odot}$
β	2.65 ± 0.05
σ_b	0.128 ± 0.003
σ_f	0.20 ± 0.01
C_*	-0.48 ± 0.02
δ	-0.06 ± 0.02
γ	0.21 ± 0.01
L'	$(3.2 \pm 1.7) \times 10^9$ L$_{\odot}$

Table A2. Parameter Pearson correlation matrix for $\Phi(L, C)$ using the C03 dual power-law form of the luminosity function (see Table A1).

	ρ_*	α	L_*	β	σ_b	σ_f	C_*	δ	γ	L'
ρ_*	1.00	−0.88	−0.93	−0.24	0.03	0.03	−0.02	0.04	0.06	0.05
α		1.00	0.73	−0.13	0.05	0.00	−0.04	−0.06	−0.18	−0.13
L_*			1.00	0.49	−0.10	−0.02	0.08	−0.00	0.04	0.03
β				1.00	−0.23	0.03	0.17	0.10	0.31	0.22
σ_b					1.00	0.09	−0.77	−0.74	−0.71	−0.76
σ_f						1.00	−0.45	−0.29	−0.39	−0.47
C_*							1.00	0.92	0.75	0.94
δ								1.00	0.67	0.83
γ									1.00	0.89
L'										1.00

Table A3. Maximum-likelihood parameter values and 1σ uncertainties for $\Phi(L, C)$ (equation 5) using the Saunders et al. (1990) form of the luminosity function [equation 7 and equations 8–10 for $p(C|L)$].

Parameter	Value
ρ_*	$(6.29 \pm 0.64) \times 10^{-3} \, \mathrm{Mpc}^{-3} \, \mathrm{dex}^{-1}$
α	1.59 ± 0.03
L_*	$(3.99 \pm 0.53) \times 10^{9} \, \mathrm{L}_\odot$
σ	0.60 ± 0.01
σ_b	0.127 ± 0.004
σ_f	0.20 ± 0.01
C_*	-0.47 ± 0.03
δ	-0.05 ± 0.02
γ	0.22 ± 0.01
L'	$(3.8 \pm 2.5) \times 10^{9} \, \mathrm{L}_\odot$

Table A4. Parameter Pearson correlation matrix for $\Phi(L, C)$ using the Saunders et al. (1990) luminosity function (see Table A2).

	ρ_*	α	L_*	σ	σ_b	σ_f	C_*	δ	γ	L'
ρ_*	1.00	−0.73	−0.98	0.83	0.27	0.33	−0.34	−0.33	−0.31	−0.38
α		1.00	0.75	−0.34	0.09	−0.11	0.01	0.07	−0.09	0.02
L_*			1.00	−0.85	−0.23	−0.30	0.29	0.29	0.29	0.35
σ				1.00	0.33	0.31	−0.33	−0.29	−0.40	−0.41
σ_b					1.00	0.41	−0.78	−0.67	−0.83	−0.77
σ_f						1.00	−0.74	−0.67	−0.55	−0.67
C_*							1.00	0.92	0.83	0.93
δ								1.00	0.73	0.81
γ									1.00	0.91
L'										1.00

This paper has been typeset from a TEX/LATEX file prepared by the author.